Peer-reviewed version available at *Nanomaterials* **2020**, *10*, 85; doi:10.3390/nano10010085

Article

The Influence of Synthesis Parameters on Structural and Magnetic Properties of Iron Oxide Nanomaterials

Laura-Madalina Cursaru[1,*], Roxana Mioara Piticescu[1,*], Dumitru Valentin Dragut[1], Ioan Albert Tudor[1], Victor Kuncser[2], Nicusor Iacob[2] and Florentin Stoiciu[1]

[1] National R&D Institute for Non-Ferrous and Rare Metals, INCDMNR-IMNR, 102 Biruintei blvd, 077145, Pantelimon, Ilfov, Romania; mpopescu@imnr.ro; roxana.piticescu@imnr.ro; dragutv@imnr.ro; atudor@imnr.ro; kuncser@infim.ro; nicusor.iacob@infim.ro; fstoiciu@imnr.ro

[2] National Institute of Materials Physics, Atomistilor 105bis, P.O. Box MG-7, 077125 Bucharest-Magurele, Romania; kuncser@infim.ro; nicusor.iacob@infim.ro

* Correspondence: roxana.piticescu@imnr.ro (R.M.P.); mpopescu@imnr.ro (L.M.C.) Tel.: +40-21-352-2048 (R.M.P); +40-21-352-2048 (L.M.C)

Abstract: Magnetic iron oxide particles are used for in vitro diagnostics for nearly 40 years. Due to their unique physical, chemical, thermal and mechanical properties, as well as biocompatibility and low toxicity in the human body, iron oxide nanoparticles have been used in many biomedical applications, such as contrast agents for magnetic resonance imaging, carriers for controlled drug delivery and immunoassays, but also in magnetic hyperthermia.

Our aim is to investigate the effect of pressure and temperature on the structural, thermal and magnetic properties of iron oxide nanomaterials prepared by hydrothermal synthesis. Iron oxide nanoparticles were synthesized at temperatures of 100-200°C and pressures of 20-1000 bar. It has been found that pressure influences the type of iron oxide crystalline phase. Thus, for lower pressure values (< 100 bar), iron oxide is predominantly formed as hematite, while at pressures > 100 bar, the major crystalline phase is goethite. The complex thermal analysis revealed the polymorphic changes of iron oxides at different temperatures. The existence of specific magnetite and hematite phases in all thermally treated samples are evidenced through the specific Verwey and Morin transitions highlighted by ZFC-FC (Zero Field Cooled-Field Cooled) measurements, whereas their relative content is precisely provided by Mössbauer spectroscopy.

Keywords: iron oxide nanoparticles; hydrothermal synthesis; high pressure; magnetic properties; thermal stability.

1. Introduction

Magnetic iron oxide particles are used for in vitro diagnostics for nearly 40 years. Due to the unique physical, chemical, thermal and mechanical properties of iron oxide nanoparticles, as well as their biocompatibility and low toxicity in the human body, they have been used in many biomedical applications [1-6], such as contrast agents [7] for magnetic resonance imaging (MRI), carriers for controlled drug delivery and immunoassays [8-13], and also in magnetic hyperthermia [14-23]. All these applications require the particles to be superparamagnetic at room temperature. Aggregation of nanoparticles should be avoided to prevent blockage of blood vessels. In addition, the particles stability in water at neutral pH is very important for these applications and the colloidal stability of the magnetic fluid depends on the coating materials and the particle size [24, 25]. Magnetic iron oxide nanoparticles with polymer coatings have also been used in cell separation, protein purification and organic or biochemical syntheses [26-30]. Coatings are not only used to enhance stability, but also particle functionality. On the other hand, it is known that when the size of the magnetic material is close to or smaller than the size of the characteristic parameters, the effect of small particle sizes can influence the important physical properties of nanostructures, such as

structural phase transition temperature or Neel temperature (the temperature at which an anti-ferromagnetic material becomes paramagnetic). For example, Jiang's group found that changing the size and grain size of metal and alloy can alter the phase transition temperature [31].

Ruan et al. [31] studied the thermal stability of nano-rings and nanotubes of α-Fe_2O_3 and found that it is closely related to the surface fraction of (001) plane in nanostructures. It has also been found that the different thickness of α-Fe_2O_3 nano-rings may affect their thermal stability. Recently, numerous experimental studies have been conducted to investigate the size effect on phase transitions [31]. It has also been studied the stability of hematite (α-Fe_2O_3) of various morphologies.

Most papers focused on oxidation from Fe_3O_4 to α-Fe_2O_3 or γ-Fe_2O_3 to α-Fe_2O_3, as these phase changes are found to be associated with particle size, nanostructure and other factors. The quasi-cubic phase stability of α-Fe_2O_3 was studied using magnetic measurements at high temperatures in high vacuum. The results showed that phase transformation from α-Fe_2O_3 (low ferromagnetic hematite) to Fe_3O_4 (ferrimagnetic magnetite) strongly depends on the size of the structures. Fe_2O_3 presents a defined chemical phase (Fe^{3+}) with high chemical stability, while the mixed chemical state of Fe_3O_4 ($Fe^{2+/3+}$) could induce instability [32].

The spectroscopic and morphological characterization of Fe_2O_3 nanowires (NWs) was performed according to calcination temperature to assess the thermal stability of NWs and temperatures over which a chemical reduction of Fe ions occurred. Thermogravimetric measurements clearly show the reduction in mass due to oxygen loss, while infrared and photoemission measurements allow tracking of the reduction of iron ions at different temperatures, indicating chemical reduction to Fe_3O_4 starting at moderate temperatures (above 440 K).

According to literature data, magnetite nanomaterials are very vulnerable to oxidation in air at temperatures above 150°C. During heating in the presence of oxygen, magnetite nanoparticles are transformed into maghemite and then into hematite. A similar effect of magnetite oxidation can be induced by laser irradiation [33, 34]. At macroscopic level, oxidation of magnetite to hematite at room temperature is inhibited and changes in the crystalline structure can be achieved only by heating at 600°C. At nanometric level, changes in crystalline structure can be expected and observed at much lower temperatures even close to room temperature. This is due to enthalpy and activation energy, which depend on particle size.

It was found that Fe nanoparticles are oxidized to a mixture of iron oxides (γ-Fe_2O_3 and α-Fe_2O_3) even at 200°C. However, this temperature may vary due to the large surface area and the various activities of the nanoparticles, which leads to a higher exothermic process during low temperature oxidation. In general, it can be assumed that phase transformations in nano-granular systems occur from 200°C to 600°C with different contributions of oxides, γ-Fe_2O_3 and α-Fe_2O_3. It should also be emphasized that data on the behavior of nanosystems in high-temperature conditions are very different and generalizations cannot be made [35].

To our knowledge, there have been no investigations regarding the effect of high pressure on the formation and phase transformations of iron oxides in aqueous environments under hydrothermal conditions. In our previous work [36], the influence of the main synthesis parameters (temperature, time, pressure) on the formation of nanosized Fe_2O_3 particles has been studied up to pressure of 20 bar.

In the present study, our aim is to investigate the effect of pressure (up to 1000 bar) and temperature, as main hydrothermal synthesis parameters on the formation of different crystalline phases of nanostructured iron oxides and on structural, thermal and magnetic properties of iron oxide nanomaterials.

2. Materials and Methods

2.1. Hydrothermal synthesis of hematite

$FeCl_3*6H_2O$, p.a, 99% (Merck), and ammonia solution (Chimreactiv) were used for hydrothermal synthesis of iron oxides.

In a first step, $FeCl_3*6H_2O$ was dissolved in distilled water to obtain a solution whose iron concentration was determined by the ICP-OES method. For the precipitation of the iron oxide precursors, a 25% ammonia solution was added dropwise under magnetic stirring. A brown precipitate with alkaline pH was obtained. Thus obtained suspension was washed to remove the by-products.

In the second step, the washed suspension (iron oxide precursor) was transferred to the autoclave and subjected to hydrothermal synthesis at 200°C for 3 hours. SAM autoclave (Romania) endorsed with cooling system, was used to prepare samples at pressures of 20-100 bar (experimental conditions: working volume 0.3 L; pressure created inside the stainless steel vessel of the autoclave using argon gas; temperature 200°C), while HP Systems autoclave (France) was used in the case of sample obtained at 1000 bar (experimental conditions: working volume 1L; isostatic pressure; temperature 100°C). After hydrothermal treatment, the nanostructured powders were dried by lyophilization using a Martin Christ Alpha 1-2 LD Plus freeze dryer. Experimental parameters of the investigated samples and chemical analysis results are presented in Table 1. Fe content was determined using chemical quantitative method, according to STAS 1574/3-90.

Table 1. Synthesis conditions and Fe content of the investigated samples

Sample name	Synthesis conditions	Material structure	Fe, wt %
NV4	200°C/3h/20 bar	hematite	68.87
NV5	200°C/3h/60 bar	hematite	68.41
NV6	200°C/3h/100 bar	hematite	68.32
NV7	100°C/3h/1000 bar	hematite/goethite	61.74

2.2. Characterization methods

The crystal structure and the phases present in the synthesized nanopowders were analyzed using X-ray phase analysis. XRD patterns were obtained by Bruker-AXS D8 ADVANCE diffractometer equipped with CuKα radiation source and a scintillation detector with graphite monochromator in vertical geometry θ-θ. XRD patterns were recorded in the range of $2\theta = 14°\div84°$ at the scan speed of 0.02 degrees/s, using DIFFRAC.EVA 2016 software and the ICDD PDF 4+ 2019 database. The chemical structure of the synthesized products was determined by Fourier Transform Infrared spectroscopy (FT-IR) within the scanning range of 550–4000 cm^{-1} in transmittance mode. Measurements were performed using a FT-IR ABB MB 3000 spectrometer equipped with an EasiDiff device for qualitative powder analysis. The solid sample was mixed with KBr powder so that its concentration in the mixture was 1 wt %. The mixture thus obtained is milled for 15 minutes to grind grains and obtain fine, homogeneous particles. For data acquisition, 64 scans were made at an optical resolution of 4 cm^{-1}. Experimental data processing was performed with the help of the Horizon MB™ FTIR software. An optical microscope (Carl Zeiss Microimaging Gmbh), with polarized, transmitted and reflected light, Axio Imager A1m, manufactured by equipped with digital camera for image acquisition and AxioVision Release 4.8.1 software for image processing, was employed to explore the morphology and to determine the microcrystalline phases based on color differences. For the microscopic study, the samples were embedded in EpoThin-Buehler resin,

sanded on abrasive paper and polished onto Lecloth-type cloth, soaked in a suspension of α-alumina in water. The image was captured with a Canon Power Shot A 640 digital camera, 10X digital zoom. Morphology and semi-quantitative analysis of iron oxide nanopowders was further investigated using scanning electron microscopy (SEM) coupled with Energy-dispersive X-ray analysis (EDS). SEM / EDS characterization was performed with Quanta 250 scanning electron microscope of high resolution, fully digitized, FEI (Netherlands) and an Energy-dispersive X-Ray spectrometer consisting of ELEMENT Silicon Drift Fixed Detector, and ELEMENT EDS Analysis Software Suite, manufactured by EDAX (USA). The samples were coated by gold to gain better conductivity required for high quality SEM imaging. Differential Scanning Calorimetry (DSC) was performed using a NETZSCH DSC 200F3 differential scanning calorimeter in Ar atmosphere. Worked in Al crucibles up to 590°C, with a heating rate of 10K / min and cooling of 30K / min. The processing of the experimental data was done with the help of the PROTEUS ANALYSIS software.

Differential Scanning Calorimetry coupled with thermogravimetry (DSC-TG) was performed with the Setaram Setsys Evolution apparatus under inert gas atmosphere (Ar/He), alumina crucibles, with heating rates of 10-50°/min, from room temperature to 1000°C, then 5 heating-cooling cycles up to 800°C at 30°/min (for NV5, NV7 samples) and 20°/min respectively (for NV4 and NV6 samples). The Calisto v1.097 software was used to process the experimental data.

The magnetic measurements have been performed by SQUID (Superconductin Quantum Interference Device) magnetometry. The MPMS 7T (Quantum Design) machine was used, as working under the most sensitive Reciprocal Space Option. ZFC-FC (Zero Field Cooled-Field Cooled) measurements under an applied field of 80 Oe have been performed in the temperature interval from 10 K to 300 K. In addition, magnetic hysteresis loops have been collected at 10 K and 300 K.

The Fe phase composition and local spin structure have been investigated by 57Fe Mössbauer spectroscopy using a constant acceleration spectrometer from SEECO. Mössbauer spectra at 295 K and 6 K have been acquired by inserting the sample in a close cycle cryostat (JANIS). The isomer shifts are reported relative to α-Fe.

3. Results and discussion

3.1. X-ray diffraction (XRD) characterization

The main crystalline phases identified in the iron oxide powders obtained by the hydrothermal process as well as their crystallite size are described in Table 2.

Figure 1 presents the XRD patterns of the investigated samples.

Peer-reviewed version available at Nanomaterials 2020, 10, 85; doi:10.3390/nano10010085

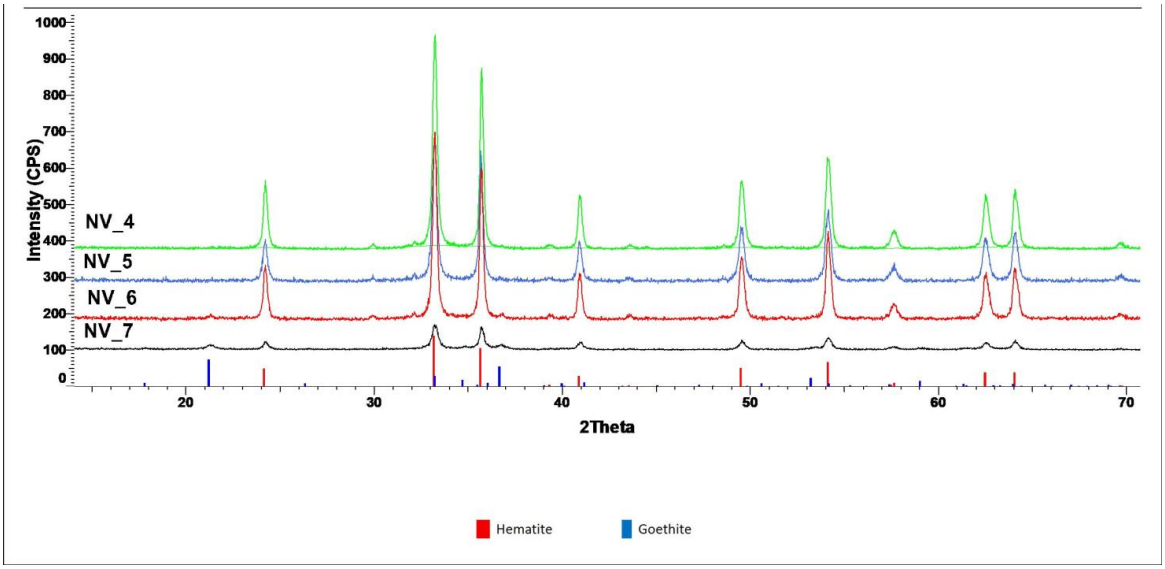

Figure 1. XRD patterns of samples NV4, NV5, NV6, and NV7

X-ray diffraction highlights the formation of hematite as the major crystalline phase in all samples synthesized by the hydrothermal process.

The main characteristic peaks of hematite (Fe_2O_3) were identified at 2θ= 33.165°, which corresponds to the (104) diffraction plane and at 2θ=35.608°, corresponding to the (110) diffraction plane. The small peak visible at 2θ=21.24° is attributed to the goethite structure, FeO(OH) structure corresponding to the (110) plane.

The crystallite sizes presented in table 2 were calculated using Scherrer formula and the values represents the sizes on the (104) – growth direction (hematite) and (110) growth direction (goethite). It is worth noting that in the case of NV6 sample, synthesized at a pressure of 100 atm, it is observed formation of goethite as the secondary phase (~ 3%), probably due to higher working pressure compared to NV4 samples (20 atm) and NV5 (60 atm). It can be observed that the formation of FeO(OH) structure as a secondary phase is favored by pressure [37, 38]. Also, its crystallite size tends to increase with increasing pressure, while the crystallite size of the Fe_2O_3 tends to decrease.

Table 2. Crystallite size and crystalline phases determined by XRD

Sample	Crystallite size (Scherrer)	The crystalline phase identified by XRD	Formula	PDF References
NV4	36 nm	Hematite	Fe_2O_3	01-089-0599
NV5	32 nm	Hematite	Fe_2O_3	01-089-0599
NV6	37 nm 22 nm	96.7% Hematite 3.3% Goethite	Fe_2O_3 FeO(OH)	01-089-0599 01-081-0464 (I)
NV7	33 nm 25 nm	~ 66 % Hematite ~ 34 % Goethite	Fe_2O_3 FeO(OH)	01-077-9924 (*) 00-029-0713 (I)

3.2. FT-IR analysis

FT-IR analysis of iron oxide based powders is depicted in figure 2.

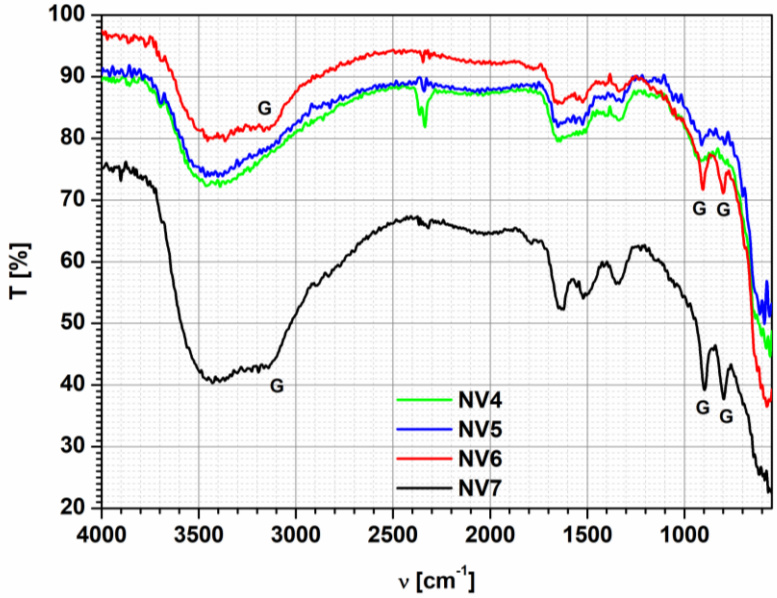

Figure 2. FT-IR spectra of samples NV4, NV5, NV6 and NV7

In the samples NV6 and NV7 the presence of the following vibration bands specific for goethite, and marked with G in Figure 4, was revealed: 905 and 800 cm^{-1} in the NV6 sample, respectively 897 and 797 cm^{-1} in the NV7 sample. Also, the stretching vibration of the O-H group at 3123 cm^{-1} in the sample NV6 and 3140 cm^{-1} in the sample NV7 is attributed to goethite, according to Betancur et al. [39]. In all the samples, one can see stretching vibration bands of the OH groups in the range 3600-3200 cm^{-1}, located on the surface of the iron oxides [8]. Also, the peaks corresponding to the deformation vibrations of the OH groups (1653 cm^{-1} for sample NV4, 1693 cm^{-1} for sample NV5, 1668 cm^{-1} for sample NV6 and 1649 cm^{-1} for sample NV7) are revealed. The stretching vibration of the OH group specific to the hematite structure at 3362 cm^{-1} in the NV6 sample confirms the results obtained by XRD analysis according to which this sample is a mixture of hematite and goethite. Also, the characteristic bands of Goethite in the NV7 sample confirm the hypothesis formulated based on the UV-VIS results, NV7 having a crystalline structure predominantly composed of goethite. The bands in the range 1335-1524 cm^{-1} observed especially in the samples NV4, NV6 and NV7 are probably due to carbonation of the powders, the band at 1335 cm^{-1} being assigned to the $(HCO_3)^-$ group and the band at 1524 cm^{-1} to the group of $(CO_3)^{2-}$ [40]. Specific Fe-O hematite vibration occurs in NV4 sample at 646 cm^{-1} and NV7 at 644 cm^{-1}, respectively.

3.3. Optical microscopy characterization (OM)

As one can observe in Figure 3, the samples consist of aggregates made of microcrystalline material, hematite α-Fe_2O_3 and possible iron oxy-hydroxides such as goethite α-FeO(OH). Sample NV4 consists mainly of hematite, represented by the red areas in figure 3a, while the goethite is present in very small quantity, being represented by the gray areas on the edge. In accordance with XRD

Peer-reviewed version available at Nanomaterials 2020, 10, 85; doi:10.3390/nano10010085

results, the presence of goethite (gray areas) can be observed in the case of sample NV6 next to white granules of hematite. The white color of hematite is explained by formation of larger-sized particles. The characteristic blood-red color of the hematite is specific to small granules and can be observed in the case of NV7 sample. The more abundant internal reflection is due to both phases (hematite and goethite). Less abundant internal reflexes can be observed in sample NV5. Particle granulation may be higher. Color effects may also be due to anisotropy [41-44].

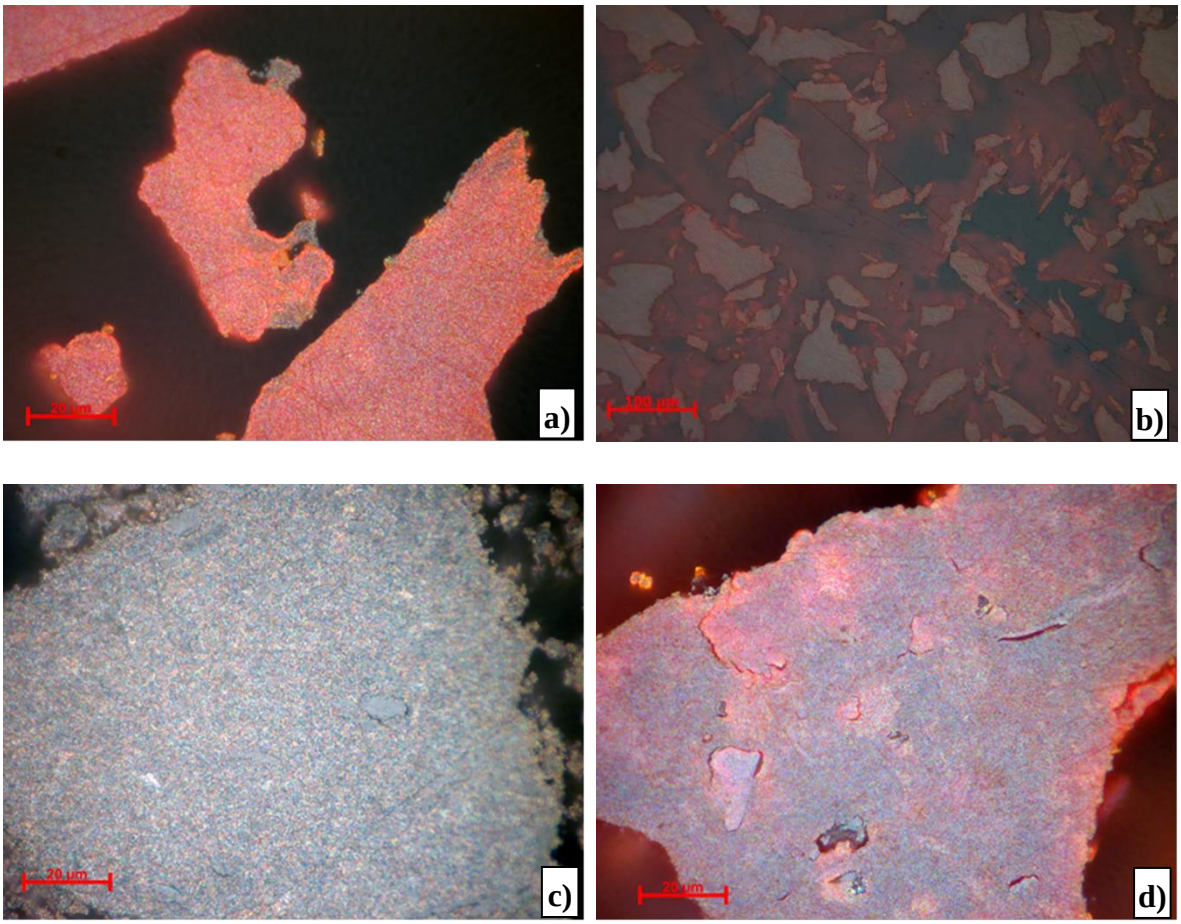

Figure 3. Reflected light. Microcrystalline aggregates in the sample: a) NV4; b) NV5; c) NV6; d) NV7

3.4. SEM-EDS characterization

The existence of hematite as major phase in hydrothermally synthesized samples is also demonstrated by SEM-EDS characterization, whereas goethite may appear as a secondary phase. An example of phase distribution inside NV4 sample is shown in figure 4.

In figure 4a, goethite phase is represented by some small light gray areas inside hematite.

Figures 4b and 4d show the distribution of O and Fe content along the line starting from the hematite predominant area (H) to a small goethite area (G). It can be seen that both oxygen and iron content are relatively constant, suggesting that NV4 sample consists of almost 100 % hematite, as resulted from XRD characterization.

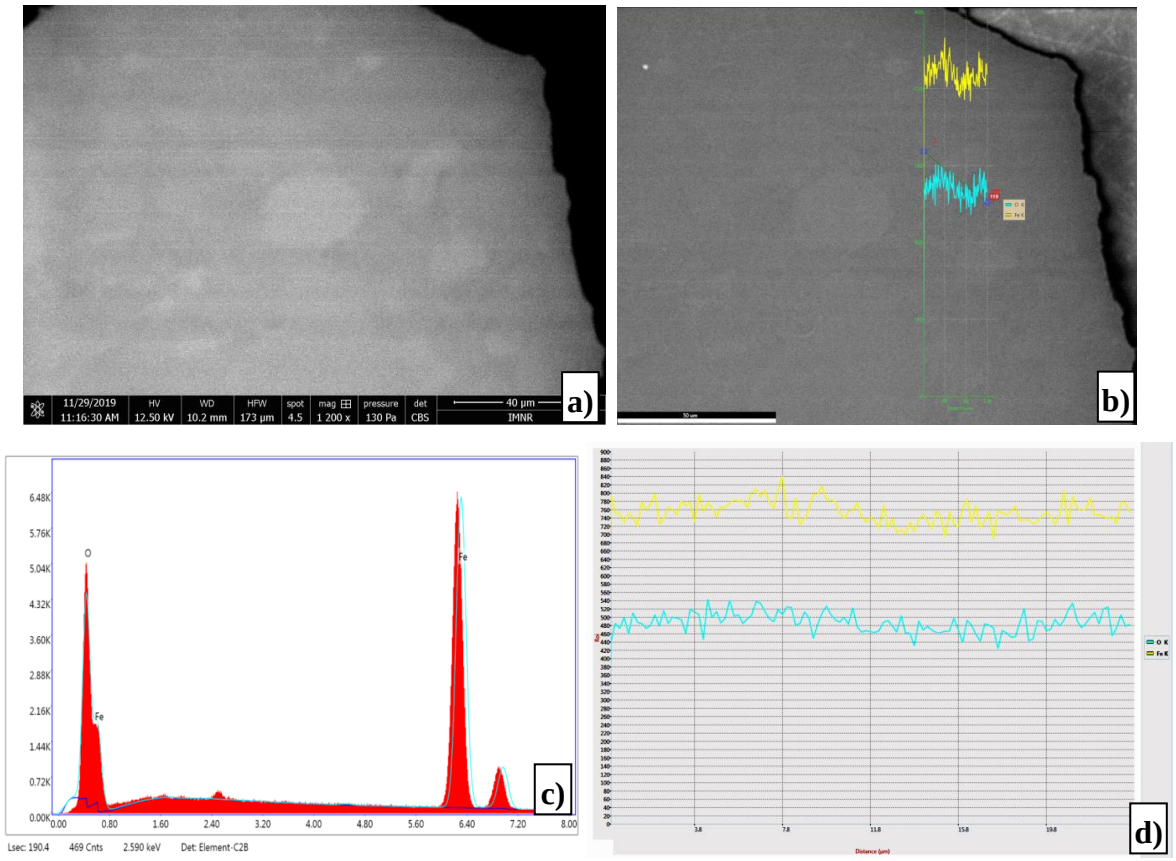

Figure 4. SEM – EDS characterization of NV4 sample: a) SEM image; b) line between hematite and goethite areas; c) EDS spectrum; d) distribution of O and Fe content along the line from left to right.

3.5. DSC analysis

The results of the DSC analysis are shown schematically in Table 3.

Table 3. Thermal analysis results (DSC method)

Sample	Peak 1		Peak 2		Peak 3		Peak 4		Peak 5	
	T, ^{0}C	ΔH, J/g	T, ^{0}C	ΔH, J/g	T, ^{0}C	ΔH, J/g	T, ^{0}C	ΔH, J/g	T, ^{0}C	ΔH, J/g
NV4	39.7	2.4	148.6	0.97	308.7	-10.7			478.9	-4.56
NV5	40.7	2.05	67.1	1.6	292.4	-0.88	366.2	-1.13	441.8	-1.33
NV6	84.5	1.65			231.2	-0.64	338.9	-3.32		
NV7	100.6	82.86	241.1	9.06	296	5.21			413.1	-21.47

Endothermic peaks in the range of 39.7-100.6°C are due to water desorption, while endothermic peaks at 148.6°C (sample NV4) and 241.1 C (sample NV7) are due to dehydration of the powder. Another endothermic peak observed in sample NV7 at 296°C could be attributed to decomposition of goethite into hematite. The exothermic peak at 231.2°C corresponding to the NV6 sample could be explained by the removal of structural water adsorbed physically on the surface of the oxide.

Exothermic peaks ranging from 338.9-478.9°C are probably due to polymorphic transformations from γ-Fe_2O_3 (maghemite) into α-Fe_2O_3 (hematite). These transformations could take place in several steps, from 292.4 (in the case of the NV5 sample) and 308.7°C (in the case of the NV4 sample) because of the nanometric dimensions, knowing that the nanoparticles have a different thermal behavior compared to the classical materials.

3.6 Complex thermal analysis characterization (DSC-TG)

The results of the DSC-TG analysis are shown schematically in Table 4.
Exothermic maxima occur in temperature range 250-340°C (probably due to secondary compounds or unreacted precursors) and 450-550°C (probably due to polymorphic transformation γ-Fe_2O_3 to α-Fe_2O_3). In addition to the endothermic maximum due to water loss (57-137°C), another endothermic effect occurs at 680°C, regardless of the heating rate, representing the Curie temperature of the hematite [45]. In order to compare the crystalline phases and crystallite sizes of iron oxides before and after thermal treatment at 680° C, the resulted powders were subjected to morpho-structural characterization.

Table 4. Results obtained by simultaneous thermal analysis DSC-TG

Sample	Speed	Peak 1		Peak 2		Peak 3		Peak 4		Peak 5	
	°/min	T, °C	ΔH, J/g	T, °C	ΔH, J/g	T, °C	ΔH, J/g	T, °C	ΔH, J/g	T, °C	ΔH, J/g
NV4 5cycles with 20°/min up to 800°C	10	57.04	5.96	**291.44**	**-9.19 exo**					676.29	0.30
	Δm, %	-0.476		**-0.222**						-0.041	**-1.578**
	20			**258.56**	**-1.63 exo**			**516.69**	**-2.07 exo**	678.41	0.33
	Δm, %			**-0.131**				**-0.027**		-0.044	**-1.794**
	30	91.38	5.86	**320.72**	**-2.73 exo**	389.34	-0.13 exo	449.94	0.39	677.92	0.30
	Δm, %	-0.59		**-0.168**		-0.035		-0.053		-0.036	**-1.686**
	50	84.29	0.27	339.48	0.28					679.23	0.38
	Δm, %	-0.167		-0.101						-0.018	**-1.737**
NV5 5cycles with 30°/min up to 800°C	10	70.79	7.10	257.45	0.72					680.94	0.26
	Δm, %	-0.395		-0.152						-6.25*10^{-3}	**-1.556**
	20	92.83	5.56	**299.67**	**-5.22 exo**	380.17	-0.55 exo	**466.56**	**-0.56 exo**	678.68	0.39
	Δm, %	-0.537		**-0.255**		-0.057		**-0.041**		-0.043	**-1.546**
	30	106.47	21.87	**273.97**	**-1.08 exo**	370.96	-8.15 exo	**512.55**	**-1.51 exo**	679.26	0.36
	Δm, %	-0.803		**-0.095**		-0.32		**-0.126**		-0.039	**-1.751**
	50	121.51	17.05							680.32	0.58

Preprints (www.preprints.org) | NOT PEER-REVIEWED | Posted: 4 December 2019 doi:10.20944/preprints201912.0036.v1

Peer-reviewed version available at Nanomaterials 2020, 10, 85; doi:10.3390/nano10010085

	Δm, %	-0.686								-0.018	**-1.501**
NV6 5cycles with 20°/min up to 800°C	10	67.72	4.35	**278.29**	**-7.76 exo**			**479.11**	**-6.27 exo**	679.00	0.38
	Δm, %	-0.368		**-0.49**				**-0.121**		-0.028	**-1.513**
	20	94.50	4.73			375.16	-14.00 exo	**499.98**	**-2.13 exo**	679.23	0.74
	Δm, %	-0.402				-0.573		**-0.1**		-0.04	**-1.963**
	30	104.36	6.26	**247.83**	**-0.93 exo**	390.41	-5.13 exo			679.83	0.82
	Δm, %	-0.439		**-0.156**		-0.629				-0.012	**-1.518**
	50	122.74	19.63			411.07	-3.92 exo	**557.59**	**-2.26 exo**	678.89	1.93
	Δm, %	-0.678				-0.559		**-0.032**		-0.072	**-1.562**
NV7 5cycles with 30°/min up to 800°C	10	89.29	84.66	**269.75**	**-6.93 exo**					680.95	0.26
	Δm, %	-5.821		**-1.604**						-7.88*10^{-3}	**-9.425**
	20	120.50 184.86	91.87 6.46	**297.43**	**-5.83 exo**			**469.56**	**-1.19 exo**	679.09	0.43
	Δm, %	-5.865 -0.718		**-1.462**				**-0.178**		-0.065	**-10.27**
	30	118.62	96.00	**290.07**	**-4.79 exo**					680.49	0.51
	Δm, %	-6.911		**-1.591**						-0.018	**-10.39**
	50	137.24	100.21	**302.59**	**-4.44 exo**					679.99	0.61
	Δm, %	-7.424		**-1.744**						-8.76*10^{-3}	**-10.88**

3.7 Morpho-structural characterization of thermally treated samples

a) XRD characterization

XRD patterns of samples after thermal treatment at 680°C, denoted as NVx-TT, are depicted in Figure 5, while its corresponding crystallite sizes are presented in Table 5.

Peer-reviewed version available at Nanomaterials 2020, 10, 85; doi:10.3390/nano10010085

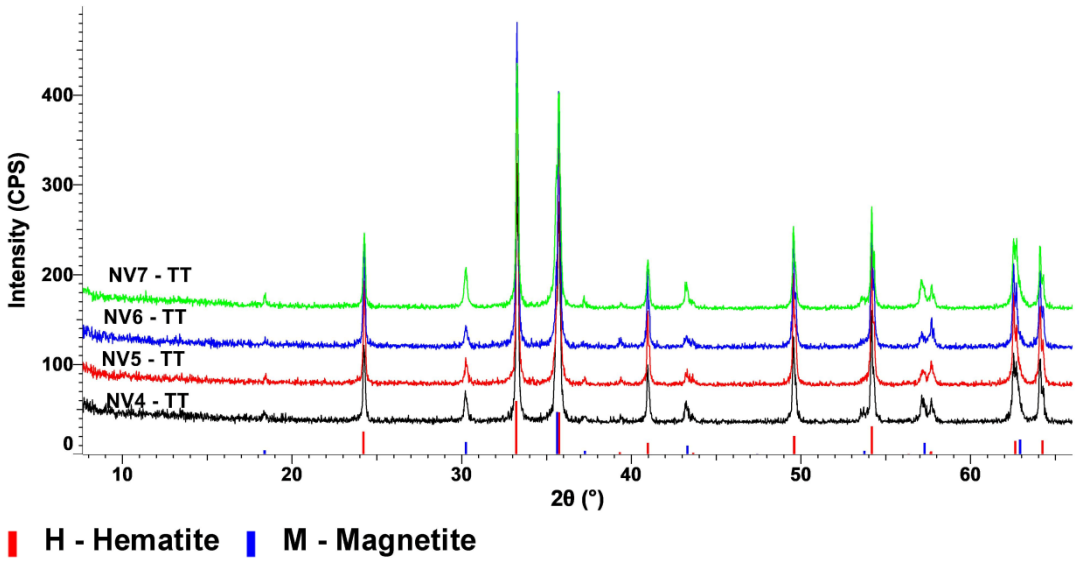

Figure 5. XRD characterization of samples NV4-TT, NV5-TT, NV6-TT, and NV7-TT

After thermal treatment at 680°C, the increasing of crystallite size (from 20-40 nm to 80-90 nm) and the partial transformartion of hematite into magnetite can be observed.

Table 5. Crystallite size and crystalline phases determined by XRD

Sample name	Pressure, bar	Crystallite size (Scherrer)	The crystalline phase identified by XRD	Formula	PDF References
NV4-TT	20	81.6 nm	Hematite Magnetite	Fe_2O_3 Fe_3O_4	PDF 04-003-5818 (P) PDF 04-007-2718 (*)
NV5-TT	60	93 nm	Hematite Magnetite	Fe_2O_3 Fe_3O_4	PDF 04-003-5818 (P) PDF 04-007-2718 (*)
NV6-TT	100	82.6 nm	Hematite Magnetite	Fe_2O_3 Fe_3O_4	PDF 04-003-5818 (P) PDF 04-007-2718 (*)
NV7-TT	1000	86.4 nm	Magnetite Hematite	Fe_3O_4 Fe_2O_3	PDF 04-007-2718 (*) PDF 04-003-5818 (P)

b) Optical microscopy characterization

Optical microscopy images of the thermally treated samples are presented in Figure 6.

The resulted obtained from optical microscopy are in agreement with XRD analysis, showing that after thermal treatment, samples consisted of: tens of % hematite and % magnetite in the case of NV4 sample; ~50% hematite and 50% magnetite for NV5 sample;

Tens of % hematite in the case of NV6 sample; and tens of % magnetite and % hematite for NV7 sample. In the case of NV4-TT sample, intense red reflexes characteristic of hematite can be observed, while the presence of magnetite is suggested by the grey areas. In most granules, magnetite and hematite are intimately associated, but are not evenly distributed. The ratio between them is

different depending on the area [41-44]. For NV5 sample, predominant areas of hematite (red color) and magnetite (grey color) are clearly delimited.

In sample NV 6, the distribution of magnetite on cracks is observed (figure 6c). Larger hematite granules (white color) are formed in NV7 sample (figure 6d). The presence of magnetite phase is confirmed by the gray areas. The two phases are relatively homogenous and uniformly distributed.

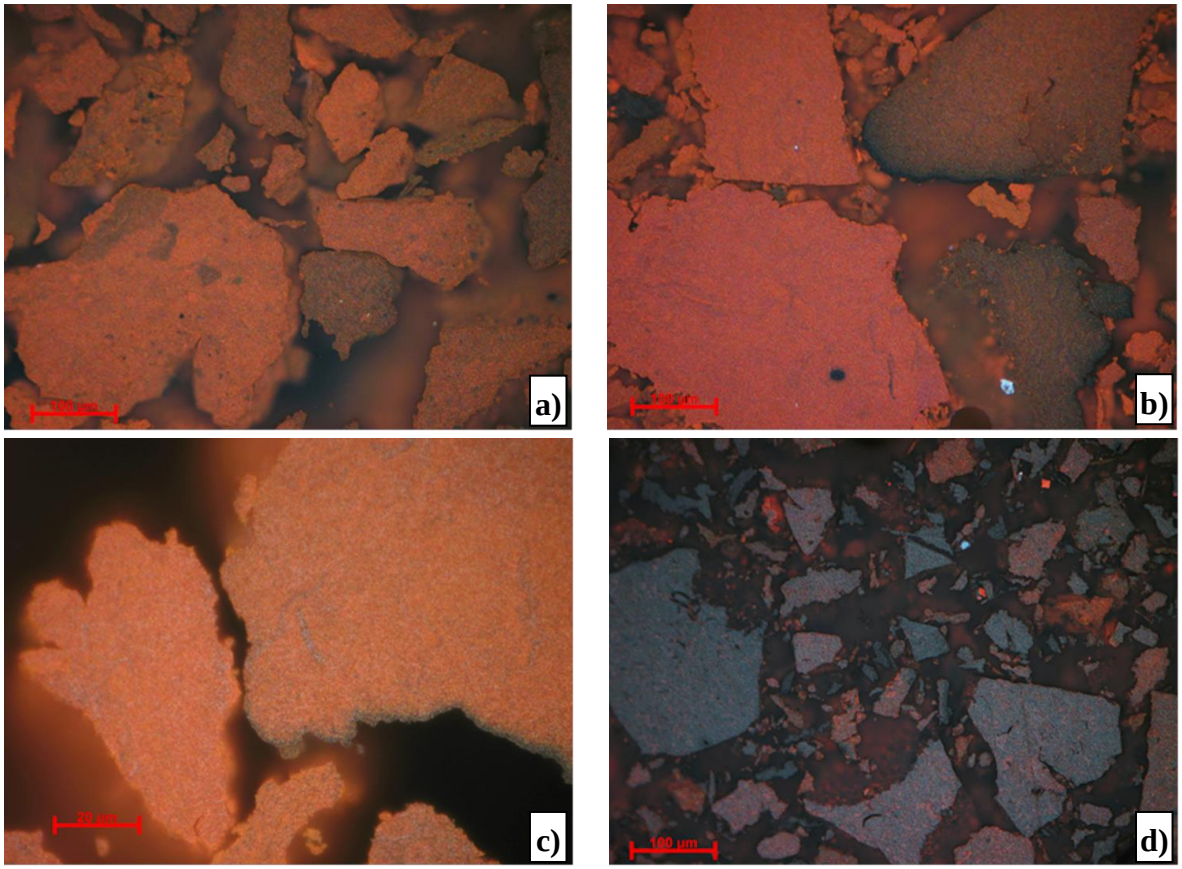

Figure 6. Reflected light. Optical micrographs of the thermally treated samples: a) NV4-TT;b) NV5-TT; c) NV6-TT; d) NV7-TT

c) SEM-EDS characterization

The existence of both hematite and magnetite phases in thermally treated samples is also demonstrated by SEM-EDS characterization. An example of phase distribution inside NV4-TT sample is shown in figure 7. In figure 7a, magnetite phase is represented by the small white areas and the cracks formed due to hematite reduction. Figures 7b and 7d clearly show the distribution of O and Fe content along the line starting from the hematite predominant area (M) to magnetite predominant area (H). It can be seen that the oxygen content decreases with the transition from H (30% O) to M (27.6%), as expected.

Preprints (www.preprints.org) | NOT PEER-REVIEWED | Posted: 4 December 2019 doi:10.20944/preprints201912.0036.v1

Peer-reviewed version available at Nanomaterials 2020, 10, 85; doi:10.3390/nano10010085

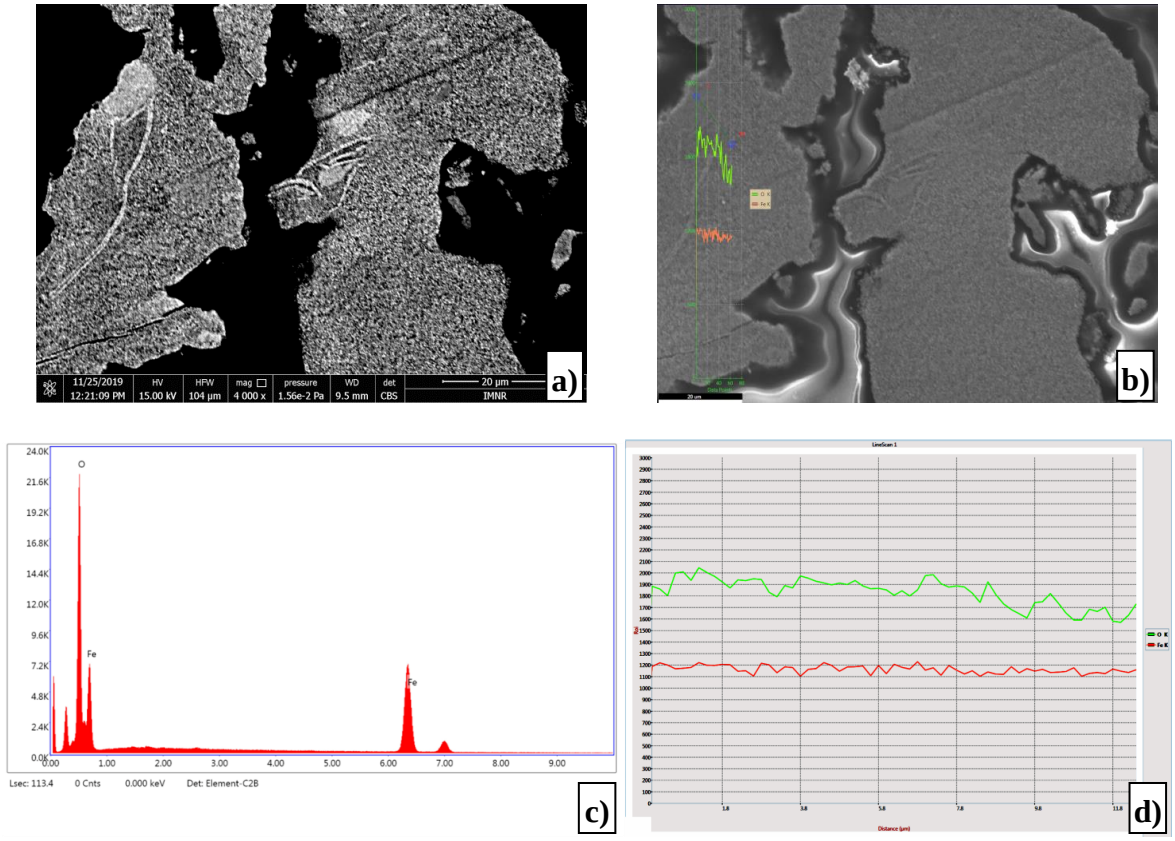

Figure 7. SEM – EDS characterization of NV4-TT sample: a) SEM image; b) line between hematite and magnetite areas; c) EDS spectrum; d) distribution of O and Fe content along the line from left to right

3.8 Magnetic characterization

ZFC-FC curves and hysteresis loops at 10 K and 300 K are shown in Figures 8 and 9 for samples NV4 and NV4-TT. As a direct observation related to sample NV4 is the step-like increment of the magnetization in the ZFC curve at about 250 K and the permanently higher magnetization in the FC curve as compared to the ZFC one. The first aspect is related to the well-known Morin transition tacking place in the corundum structure of hematite, pointing to a change in the spin structure from antiferromagnetic (at low temperature) to a weak ferromagnetic one at room temperature [46]. To note that such a transition assumes a well crystallized hematite with nanoparticle size ranging out from the superparamagnetic regime. However, the upper variation of the FC curve over the ZFC one supports the idea of monodomain like nanoparticles, in agreement with sizes of tenths of nanometers as obtained from XRD. The change from an antiferromagnetic spin structure at low temperature to a week ferromagnetic one at room temperature is related to the appearance of a slight canting along the [111] trigonal direction of the spins initially antiferomagnetic coupled in the (111) plane at low temperature. The main antiferromagnetic behavior is also sustained by the lack of saturation with continuous (linear) increment of the magnetization in higher fields as well as by the very low values of magnetization whereas the above mentioned change in the spin structure is sustained by the higher magnetization in the loop at 300 K as compared to the loop at 10 K (see Figure 8, left side).

Preprints (www.preprints.org) | NOT PEER-REVIEWED | Posted: 4 December 2019 doi:10.20944/preprints201912.0036.v1

Peer-reviewed version available at Nanomaterials 2020, 10, 85; doi:10.3390/nano10010085

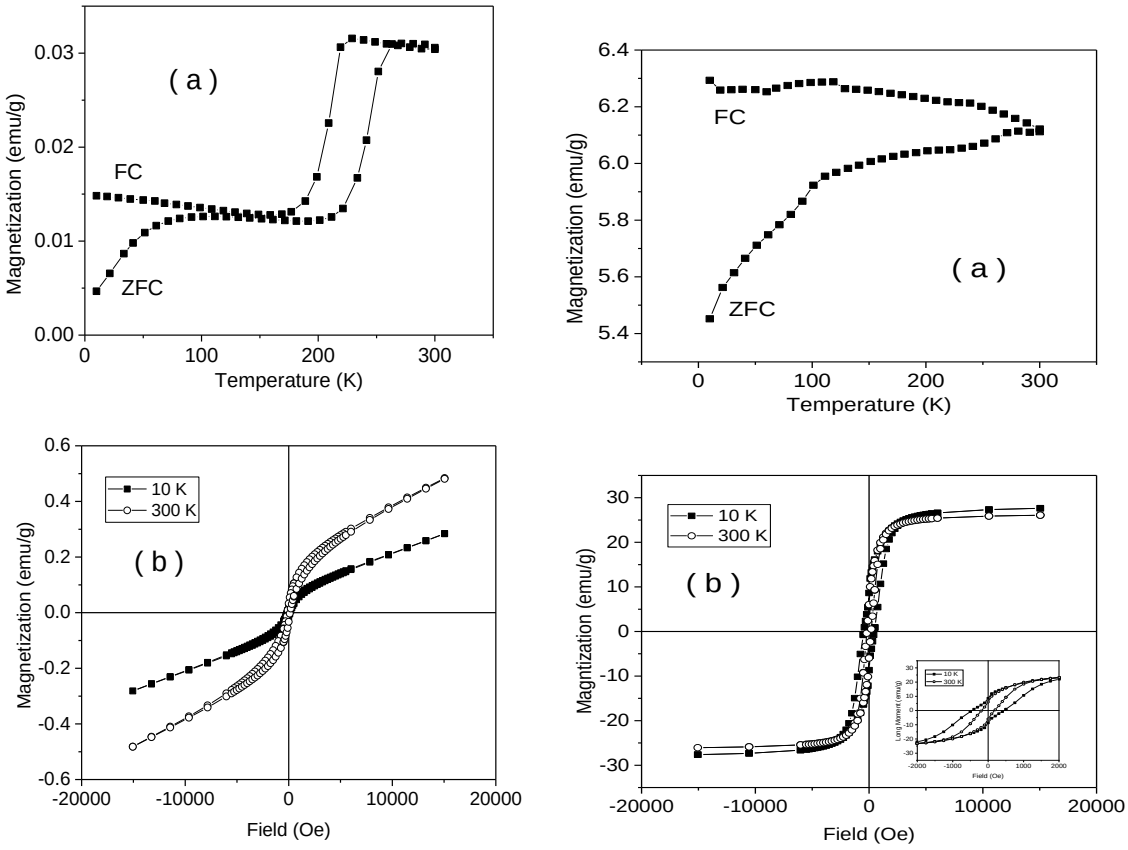

Figure 8. ZFC-FC curves collected in 80 Oe DC applied field (a) and hysteresis loops (b) for sample NV4 (left side) and sample NV4-TT (right side), respectively.

To note the drastically changed ZFC-FC curves and hysteresis loops of sample NV4-TT as compared to the case of sample NV4 (see Figure 8, right side). First of all, the branching aspect with continuous increase of the ZFC curve vs temperature and continuous increase of FC magnetization at decreasing temperature stand for magnetic mono-domain nanoparticles with blocking temperatures well above 300 K. The small jumps on both ZFC and FC curves evidenced in the range of 100-120 K and 230-250 K suggest the formation of poorly crystallized magnetite phases (with Verwey temperature of about 120 K) and a rest of hematite nanoparticles (with a Morin temperature of about 250 K). Definitely, this aspect is also supported by the value of saturation magnetization, e.g. about 28 emu/g at 10 K as resulting from the loops presented in Figure 8(b), right side. Assuming that a well crystallized magnetite might have some 90 emu/g saturation magnetization, it results a roughly amount of maximum 28% of magnetite in the sample. In inset of the same figure are presented the loops over a narrower field range, pointing for the presence of 2 magnetic phases, the one giving the dominant magnetic signal having a coercive field of about 450 Oe at 10 K and 190 Oe at 300 K, specific to magnetite.

The magnetic measurements obtained on samples NV6 and NV6-TT are shown in Figure 9. The first aspect derived from ZFC-FC measurement is the lack of any trace of nanoparticle related dynamical behavior of superspins in the NV6 system (e.g. no increment of the ZFC curve at low temperature).

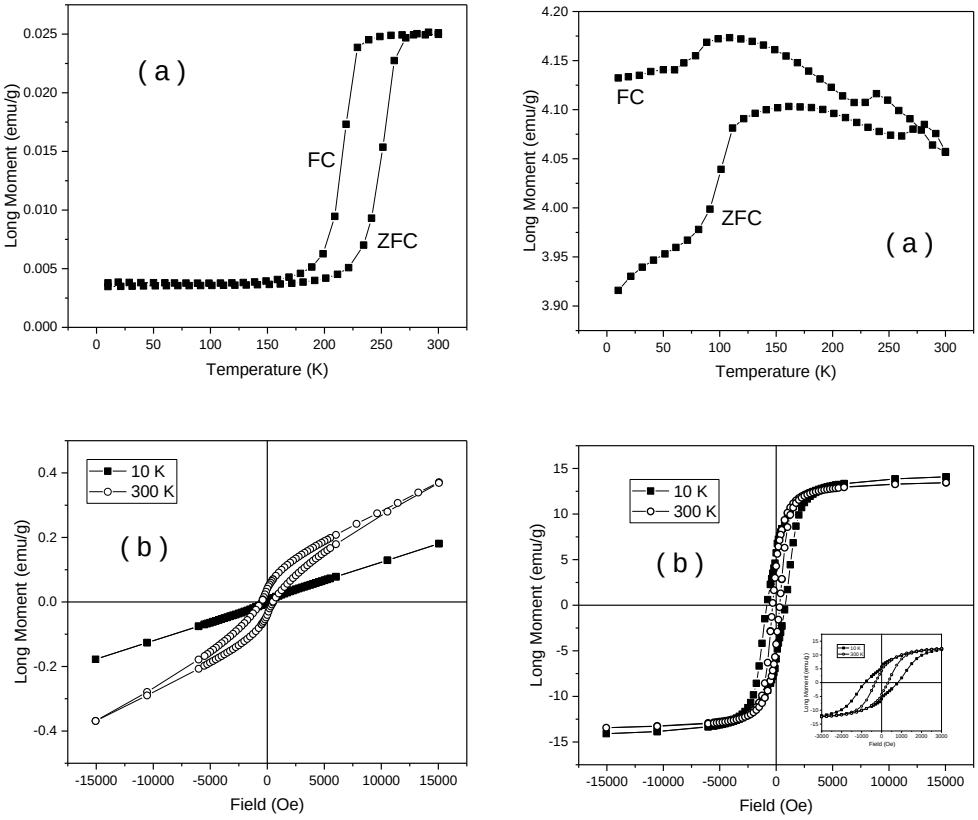

Figure 9. ZFC-FC curves collected in 80 Oe DC applied field (a) and hysteresis loops (b) for sample NV6 (left side) and NV6-TT (right side).

That suggests that even in a case of nanoparticle-like morphology, these interact magnetically not only by week dipolar interactions, but much stronger.

On the other hand, the Morin transition is very clearly evidenced in this sample together with its interesting temperature loop (Figure 9 (a) and (b), left side). It is to be concluded that well-formed and strongly interacting hematite particles are found, giving rise to an overall structure of magnetic domains at 300 K, as evidenced via the corresponding hysteresis loop in Figure 9 (b).

To note the same characteristics of the hysteresis loops for this sample as for sample NV4, except a much larger coercive field at 300 K (e.g. 500 Oe as compared to 140 Oe, in case of negligible coercive fields at 10 K.

The thermal annealing changes again the phase composition as clearly evidenced from Figure 9 (a), left side, where again two magnetic transitions can be deduced from both ZFC and FC curves (the Verwey transition at 100 -120 K and Morin transition at 220-260 K). Both transitions are much better evidenced as compared to sample NV4-TT (see Figure 9 (a)) in conditions of a much lower magnetization at saturation of only 15 emu/g at 10 K (see Figure 9 (b)) This means that the amount of magnetite is lower in sample NV6-TT (e.g. less than 17 %), but it is of much better quality (e.g. better crystallized) than in case of sample NV4-TT. This fact is supported also by the enhanced coercive fields in this sample, e.g. of 840 Oe at 10 K and 320 Oe at 300 K.

Finally, the magnetic results on samples NV7 and NV-7TT are shown in Figure 10.

The first aspect to be mentioned is the higher magnetization and the trend of the ZFC curve of NV7 sample (Figure 10 (a), left side) with a maximum at a temperature of about 50 K specific to

nanoparticulate systems with enhanced magnetic moments (e.g. no antiferromagnetic coupling) and a blocking temperature of 50 K. However, the type of branching supports also the presence of an additional magnetic phase which intermediates a sort of inter-particle interactions. The magnetization values in high fields are, according to Figure 10 (b), left side, an order of magnitude higher than in case of the previous samples, giving support for a magnetic phase different from hematite. This additional phase which is magnetic at low temperatures and with paramagnetic/superparamagnetic behaviour at 300 K can be assigned to a Fe oxo-hydroxide, which nature might be better determined by Mössbauer spectroscopy.

Finally, following the thermal treatment, the specific magnetite and hematite phases are again evidenced through the specific Verwey and Morin transitions evidenced by the ZFC-FC measurements on sample NV7-TT (Figure 10(a), right side). The saturation magnetization is close to 30 emu/g (at both 10 K and 300 K), proving quite large magnetite particle sizes). Together with the well pronounced jump along the Verwey transition, this result supports the formation of well crystallized and relatively large magnetite nanoparticles with a relative concentration close to 33 wt. %.

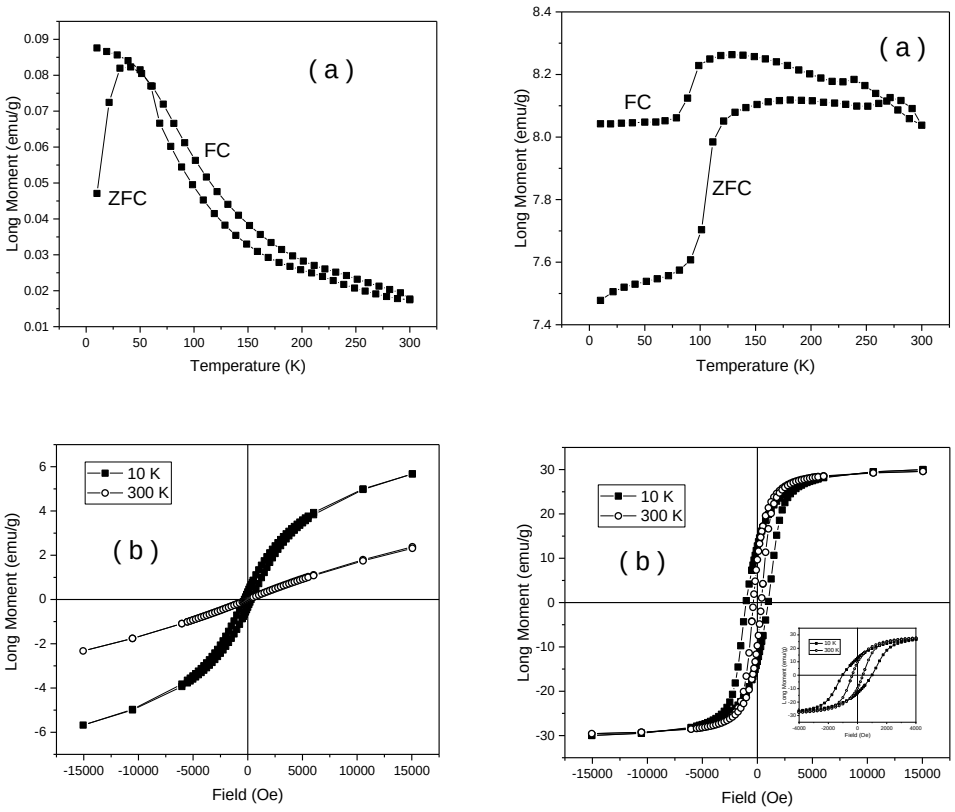

Figure 10. ZFC-FC curves collected in 80 Oe DC applied field (a) and hysteresis loops (b) for sample NV7 (left side) and NV7-TT (right side).

Mössbauer spectra of samples NV4 and NV4-TT (at 6 K and 300 K for each sample) are shown in Figure 11 (a and b for NV4; c and d for NV4-TT). Mössbauer spectra of samples NV5, NV6 and NV7 (at 10 K and 300 K for each sample) are shown in Figure 12 (a, b for NV5; c, d for NV6; and e, f for NV7). It can be observed that the as prepared sample NV4 consists at 6 K and 300 K in only one sextet component with hyperfine parameters specific to hematite (e.g. hyperfine magnetic field of 54

T at 6 K and 51 T at 300 K). After the thermal treatment an additional phase fitted by one Mössbauer sextet at 6 K and two Mossbauer sextets at 300 K are observed. The hyperfine parameters of this new phase are specific to magnetite (e.g. at 300 K the hyperfine magnetic fields are of 49.2 T and 46.3 T). The magnetite represents 24% from the Fe phases, the rest of 76% remaining as hematite. To note the very defect structure of magnetite with an occupation of 1:1 on octahedral to tetrahedral positions.

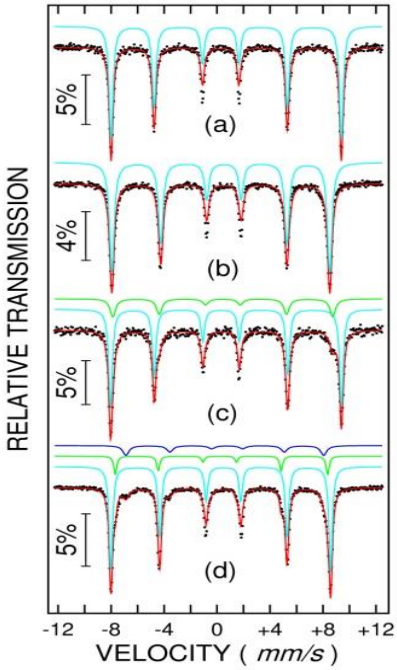

Figure 11. Mössbauer spectra of sample NV4 at 6 K and 300 K (a and b) and NV4-TT (c and d).

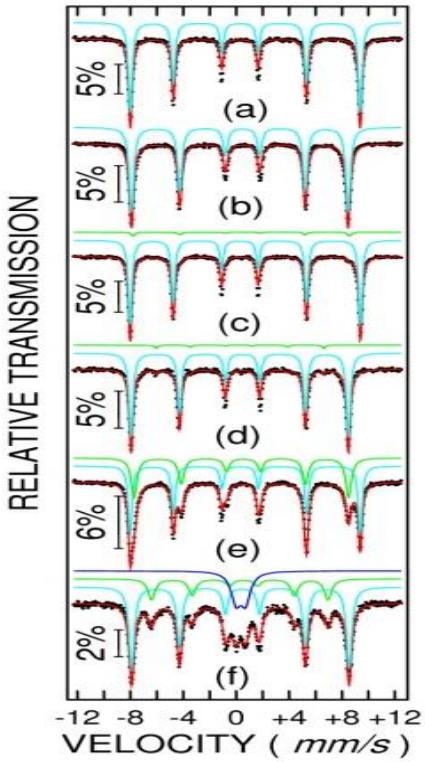

Figure 12. Mössbauer spectra of sample NV5 at 6 K and 300 K (a and b), NV6 (c and d) and NV7 (e and f).

Preprints (www.preprints.org) | NOT PEER-REVIEWED | Posted: 4 December 2019 doi:10.20944/preprints201912.0036.v1

Peer-reviewed version available at Nanomaterials 2020, 10, 85; doi:10.3390/nano10010085

Concerning the behavior of the rest of as prepared samples, NV5 is also represented by only one component with specific hyperfine parameters for hematite, NV6 presents an additional component (3 wt %) with hyperfine parameters specific to goethite (e.g. 50.3 T at 6 K and 38.2 T at 300 K), in excellent agreement with the XRD characterization and finally, sample NV7 is formed by 56% of hematite and 44% of goethite, according to the low temperature Mössbauer spectrum (to note that MS is more sensitive to the composition of the Fe phases as compared to XRD). At RT, about 20% of goethite becomes superparamagnetic within the Mössbauer time window, again in excellent agreement with the magnetic measurements pointing for superparamagnetic behavior of goethite nanoparticles at higher temperatures.

The as evidenced type of involved magnetic phases and their distribution in the analyzed samples are shown in Table 6 and Figure 13.

Table 6. Phase distribution in all samples

Sample name	Phase type
NV4	hematite
NV4-TT	Hematite+magnetite
NV5	hematite
NV5-TT	Hematite+magnetite
NV6	Hematite+goethite
NV6-TT	Hematite+magnetite
NV7	Hematite+goethite
NV7-TT	Hematite+magnetite

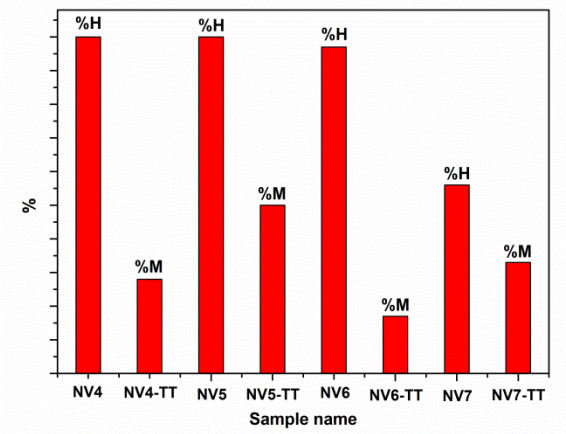

Figure 13. Distribution of hematite (H) and magnetite in all samples before and after thermal treatment

4. Conclusions

The influence of synthesis pressure on crystalline structure of iron oxide prepared by hydrothermal method was studied. It has been found that for lower pressure values (less than 100 bar), iron oxide is predominantly formed as hematite, while at pressures above 100 bar, the major crystalline phase is goethite. The complex thermal analysis by the DSC method revealed the polymorphic changes of iron oxides at different temperatures. Thermal stability of hydrothermal synthesized nanoparticles under various experimental conditions has been demonstrated by performing heating/cooling cycles.

The specific magnetite and hematite phases have been evidenced in all thermally treated samples through XRD, optical microscopy, SEM characterization and the specific Verwey and Morin transitions evidenced by the ZFC-FC measurements. ZFC and FC curves suggested the formation of poorly crystallized magnetite (maximum 28%) phases (with Verwey temperature of about 120 K) and a rest of hematite nanoparticles (with a Morin temperature of about 250 K) in the case of NV4-TT sample. The amount of magnetite is lower in sample NV6-TT (e.g. less than 17 %), but it is much better crystallized than in case of sample NV4-TT. The formation of well crystallized and relatively large magnetite nanoparticles with a relative concentration close to 33 wt. % was observed in the

case of NV7-TT sample. The formation of well crystallized magnetite in thermally treated samples increases with pressure increase. The results obtained in Mössbauer characterization are in excellent agreement with the XRD and MO characterization, showing the formation of one component in the case of samples prepared at lower pressure (< 100 bar) – hematite (with partial transformation in magnetite after thermal treatment), and the appearance of goethite for samples synthesized at pressures > 100 bar.

Author Contributions: Conceptualization, L.M.C. and R.M.P.; Methodology, L.M.C., R.M.P., V.K. and F.S.; Investigation, D.V.D., I.A.T., N.I., F.S.; Writing – Original Draft Preparation, L.M.C.; Writing – Review & Editing, R.M.P and V.K.; Project Administration, R.M.P.; Funding Acquisition, R.M.P and V.K.

Funding: This research was funded by ERANET-EURONANOMED 2 project, acronym NANOVIBER, UEFISCDI ctr. no.1/2017 (IMNR) and PN-III-P1-1.2-PCCDI-2017-0871 (NIMP).

Conflicts of Interest: The authors declare no conflict of interest.

References

1. Magro, M.; Vianello, F. Bare Iron Oxide Nanoparticles: Surface Tunability for Biomedical, Sensing and Environmental Applications. *Nanomaterials* **2019**, *9*, 1608.
2. Mai, T.; Hilt, J. Z. Functionalization of iron oxide nanoparticles with small molecules and the impact on reactive oxygen species generation for potential cancer therapy, *Colloid Surface A*. **2019**, *576*, 9–14.
3. Morel, M. J.; Mosquera, E.; Sáez, P. Surface modification and polymerization on iron oxide nanoparticles obtained from mineral magnetite. *Surf Interfaces* **2019**, *17*, 100349.
4. Gupta, A.K.; Gupta, M. Synthesis and surface engineering of iron oxide nanoparticles for biomedical applications. *Biomaterials* **2005**, *26*, 3995–4021.
5. Rabinca, A.; Buleandra, M.; Tache, F.; Mihailciuc, C.; Ciobanu, A.; Stefanescu, D.; Ciucu, A. Voltammetric Method for Simultaneous Determination of L-Dopa and Benserazide. *Curr. Anal. Chem.* **2017**, *13*, 218-224.
6. Ciobanu, A.M.; Popa, C.; Marcu, M.; Ciobanu, C.F. Psychotic depression due to giant condyloma Buschke-Löwenstein tumors. *Rom J Morphol Embryol*. **2014**, *55*, 189-195.
7. González-Gómez, M.A.; Belderbos, S.; Yañez-Vilar, S.; Piñeiro, Y.; Cleeren, F.; Bormans, G.; Deroose, C.M.; Gsell, W.; Himmelreich, U.; Rivas, J. Development of Superparamagnetic Nanoparticles Coated with Polyacrylic Acid and Aluminum Hydroxide as an Efficient Contrast Agent for Multimodal Imaging. *Nanomaterials* **2019**, *9*, 1626.
8. Kirubha, S. P. A.; Rajput, A. Enhancement of Thermal Imaging by Iron Oxide Nanoparticle – Preliminary Study. *Biocatal Agric Biotechnol* **2019**, *17*, 352–360.
9. Abd Elrahman, A.A.; Mansour, F.R. Targeted magnetic iron oxide nanoparticles: Preparation, functionalization and biomedical application. *J Drug Deliv Sci Tec* **2019**, *52*, 702-712.
10. Roca, A.G.; Gutiérrez, L.; Gavilán, H.; Brollo, M.E.F.; Veintemillas-Verdaguer, S.; Morales, M.D. Design Strategies for Shape-Controlled Magnetic Iron Oxide Nanoparticles. *Adv Drug Deliver Rev* **2019**, *138*, 68–104.
11. Liyanage, P.Y.; Hettiarachchi, S.D.; Zhou, Y.Q.; Ouhtit, A.; Seven, E.S.; Oztan, C.Y.; Celik, E.; Leblanc, R.M. Nanoparticle-mediated targeted drug delivery for breast cancer treatment. *Bba-Rev Cancer* **2019**, *1871*, 419–433.
12. Hola, K.; Markova, Z.; Zoppellaro, G.; Tucek, J.; Zboril, R. Tailored functionalization of iron oxide nanoparticles for MRI, drug delivery, magnetic separation and immobilization of biosubstances. *Biotechnol Adv* **2015**, *33*, 1162–1176.

13. Mahmoudi, M.; Sant, S.; Wang, B.; Laurent, S.; Sen, T. Superparamagnetic iron oxide nanoparticles (SPIONs): Development, surface modification and applications in chemotherapy. *Adv Drug Deliver Rev* **2011**, *63*, 24–46.
14. Hu, H.; Yuan, Y.; Lim, S.; Wang, C.H. Phase structure dependence of magnetic behaviour in iron oxide nanorods, *Mater Design* **2020**, *185*, 108241.
15. Nikitin, A.; Khramtsov, M.; Garanina, A.; Mogilnikov, P.; Sviridenkova, N.; Shchetinin, I.; Savchenko, A.; Abakumov, M.; Majouga, A. Synthesis of iron oxide nanorods for enhanced magnetic hyperthermia. *J Magn Magn Mater* **2019**, *469*, 443–449.
16. Rybka, J.D. Radiosensitizing properties of magnetic hyperthermia mediated by superparamagnetic iron oxide nanoparticles (SPIONs) on human cutaneous melanoma cell lines. *Rep Pract Oncol Radiother* **2019**, *24*, 152–157.
17. Oliveira, A.; Hneda, M.L.; Fernandez-Outon, L.E.; de Sousa, E.M.B.; Ardisson, J.D. Synthesis and characterization of nanocomposites based on rare-earth orthoferrites and iron oxides for magnetic hyperthermia applications. *Ceram. Int.* **2019**, *45*, 17920–17929.
18. Yasemian, A.R.; Kashi, M.A.; Ramazani, A. Surfactant-free synthesis and magnetic hyperthermia investigation of iron oxide (Fe3O4) nanoparticles at different reaction temperatures. *Mater. Chem. Phys* **2019**, *230*, 9-16.
19. Abenojar, E.C.; Wickramasinghe, S.; Bas-Concepcion, J.; Samia, A.C.S. Structural effects on the magnetic hyperthermia properties of iron oxide nanoparticles. *Prog Nat Sci-Mater* **2016**, *26*, 440–448.
20. Soares, P.I.P.; Laia, C.A.T.; Carvalho, A.; Pereira, L.C.J.; Coutinho, J.T.; Ferreira, I.M.M.; Novo C.M.M.; Borges, J.P. Iron oxide nanoparticles stabilized with a bilayer of oleic acid for magnetic hyperthermia and MRI applications. *Appl Surf Sci* **2016**, *383*, 240–247.
21. Ebrahimisadr, S.; Aslibeiki, B.; Asadi, R. Magnetic hyperthermia properties of iron oxide nanoparticles: The effect of concentration. *Physica C*, **2018**, *549*, 119–121.
22. Elsayed, W.E.M.; Al-Hazmi, F.S.; Memesh, L.S.; Bronstein, L.M. A novel approach for rapid green synthesis of nearly mono-disperse iron oxide magnetic nanocubes with remarkable surface magnetic anisotropy density for enhancing hyperthermia performance. *Colloid Surface A* **2017**, *529*, 239–245.
23. Gyergyek, S.; Makovec, D.; Jagodič, M.; Drofenik, M.; Schenk, K.; Jordan, O.; Kovac, J.; Drazic, G.; Hofmann, H. Hydrothermal growth of iron oxide NPs with a uniform size distribution for magnetically induced hyperthermia: Structural, colloidal and magnetic properties. *J Alloy Compd* **2017**, *694*, 261–271,
24. Wu, W.; He, Q.; Jiang, C. Magnetic Iron Oxide Nanoparticles: Synthesis and Surface Functionalization Strategies, *Nanoscale Res* Lett **2008**, *3*, 397–415.
25. Miola, M.; Ferraris, S.; Pirani, F.; Multari, C.; Bertone, E.; Žužek Rožman, K.; Kostevšek, N.; Verné, E. Reductant-free synthesis of magnetoplasmonic iron oxide-gold nanoparticles. *Ceram Int* **2017**, *43*, 15258–15265.
26. Gholamia, L.; Kazemi Oskueeb, R.; Tafaghodic, M.; Ramezani Farkhanic, A.; Darroudid, M. Green facile synthesis of low-toxic superparamagnetic iron oxide nanoparticles (SPIONs) and their cytotoxicity effects toward Neuro2A and HUVEC cell lines. *Ceram Int* **2018**, *44*, 9263–9268.
27. Buchman, J.T.; Pho, T.; Rodriguez, R.S.; Feng, Z.V.; Haynes, C.L. Coating iron oxide nanoparticles with mesoporous silica reduces their interaction and impact on S. oneidensis MR-1. *Chemosphere* **2019**, *237*, 124511.
28. Tadic, M.; Kralj, S.; Kopanja, L. Synthesis, particle shape characterization, magnetic properties and surface modification of superparamagnetic iron oxide nanochains. *Mater Charact* **2019**, *148*, 123–133.

29. Ghasemi, A.; Jafari, S.; Saeidi, J.; Mohtashami, M.; Salehi, I. Synthesis and characterization of polyglycerol coated superparamagnetic iron oxide nanoparticles and cytotoxicity evaluation on normal human cell lines. *Colloid Surface A* **2018**, *551*, 128–136.
30. Medeiros, S.F.; Filizzola, J.O.C.; Fonseca, V.F.M.; Oliveira, P.F.M.; Silva, T.M.; Elaissari, A.; Santos, A.M. Synthesis and characterization of stable aqueous dispersion of functionalized double-coated iron oxide nanoparticles. *Mater Lett* **2015**, *160*, 522–525.
31. Ruan, C.; Wang, J.; Gao, M.; Zhao, G. The influence of structural size on thermal stability in single crystalline hematite uniform nano/micro-cubes. *Mater Chem Phys* **2016**, *183*, 158-164.
32. Paolone, A.; Angelucci, M.; Panero, S.; Betti, M.G.; Mariani, C. Thermal stability and reduction of iron oxide nanowires at moderate temperatures. *Beilstein J Nanotech* **2014**, *5*, 323–328.
33. Cendrowski, K.; Sikora, P.; Zielinska, B.; Horszczaruk, E.; Mijowska E.; Chemical and thermal stability of core-shelled magnetite nanoparticles and solid silica. *Appl Surf Sci* **2017**, *407*, 391–397.
34. Barnakov, Y. A.; Yu, M. H.; Rosenzweig, Z. Manipulation of the magnetic properties of magnetite silica nanocomposite materials by controlled Stober synthesis. Langmuir **2005**, 21, 7524–7527.
35. Kalska-Szostko, B.; Wykowska, U.; Satula, D.; Nordblad, P. Thermal treatment of magnetite nanoparticles. *Beilstein J Nanotech* **2015**, *6*, 1385–1396.
36. Popescu, M.; Piticescu, R.M.; Vasile, E.; Taloi, D.; Petriceanu, M.; Stoiciu, M.; Badilita, V. The Influence of Synthesis Parameters on FeO(OH) / Fe2O3 Formation by Hydrothermal Techniques, *Z Naturforsch B*, **2010**, *65b*, 1024-1032.
37. http://www1.lsbu.ac.uk/water/physical_anomalies.html
38. Cornell, R.M.; Schwertmann, U. ***The Iron Oxides: Structure, Properties, Reactions, Occurences and Uses***, Wiley-VCH Verlag GmbH & Co. KGaA, Weinheim, Germany, 2003; pp. 365-382.
39. Betancur, A.F.; Pérez, F.R.; del M. Correa, M.; Barrero, C.A. Quantitative approach in iron oxides and oxihydroxides by vibrational analysis. *Optica Pura y Aplicada* **2012**, *45*, 269-275.
40. Lu, B. Surface Reactivity of Hematite Nanoparticles. Master Thesis 45 ECTS, **2014**.
41. Ramdohr, P. ***The Ore Minerals and their intergrowths***, 1st ed.; Pergamon Press, Braunschweig, Germany, 1969; pp. 878-1074.
42. Winchell, A.N. ***Elements of optical microscopy: an introduction to microscopic petrography***, John Wiley & Sons, New York, USA, 1965; pp. 62-136.
43. Petruk, W. ***Applied mineralogy in the mining industry***, Elsevier, Ottawa, Canada, 2000; pp149-183.
44. Ianovici, V; Stiopol, V.; Constantinescu, E. ***Mineralogie***, Editura Didactica si Pedagogica, Bucuresti, Romania, 1979.
45. Smykatz-Kloss, W. *Differential Thermal Analysis: Application and Results in Mineralogy*, Springer Science & Business Media, 2012.
46. Greenwood, N.N.; Gibb, T.G. ***Mössbauer Spectroscopy***, Chapman and Hall Ltd., London 1971.